Dual-Robotic Ultrasound System for In Vivo Prostate Tomography

Kevin M. Gilboy[1(✉)], Yixuan Wu[1], Bradford J. Wood[2], Emad M. Boctor[1], and Russell H. Taylor[1]

[1] The Johns Hopkins University, Baltimore, MD 21218, USA
kgilboy1@jhu.edu
[2] National Institutes of Health, Bethesda, MD 20814, USA

Abstract. Ultrasound computed tomography (USCT) offers quantitative anatomical tissue characterization for cancer detection. While most research and commercial development has focused on submerging target anatomy in a transducer-lined cylindrical water tank, this is not practical for imaging deep anatomy and an alternative approach using aligned abdominal and endoluminal ultrasound probes is required. This work outlines and validates a clinical workflow and real-time motion framework for a novel dual-robotic approach specific to in vivo prostate imaging: one arm wielding a linear abdominal probe, the other wielding a linear transrectal ultrasound (TRUS) probe. After calibration, the robotic system works to keep the abdominal probe collinear with the physician-rotated TRUS probe using a convex contour tracking scheme, while also enforcing its gentle contact with the patient's pubic region to capture the ultrasound slices needed for limited-angle tomographic reconstruction. The repeatable and accurate robotic system presents feasibility for prostate USCT and future malignancy diagnosis and staging in vivo.

Keywords: Ultrasound tomography · Robotic ultrasound · Prostate imaging

1 Introduction

Prostate cancer is the second leading non-cutaneous cancer and the fifth leading cause of cancer death globally for males in 2018 [4]. Due to inaccuracies and limitations of prostate-specific antigen (PSA) testing and serial blind biopsies, modern diagnostics involve a combination of PSA and transrectal ultrasound (TRUS) followed by mpMRI if there is heightened concern for cancer [17]. MRI can also be fused with real-time TRUS data to guide targeted prostate biopsy [12] which, while the de facto gold standard in prostate cancer diagnosis, is only one factor in pathology determination and is usually costly and schedule-limited. This raises the question if the initial B-Mode TRUS scan can enhance sensitivity and specificity of cancer detection, despite only a 50%–60% detection accuracy and approximate 6% positive predictive value due to undetectable isoechoic

Y. Hu et al. (Eds.): ASMUS 2020/PIPPI 2020, LNCS 12437, pp. 161–170, 2020.
https://doi.org/10.1007/978-3-030-60334-2_16

or echopoor lesions [8]. Although qualitative ultrasound (US) imaging (e.g. B-mode) is limited in precision, quantitative imaging via US computed tomography (USCT) may be eligible for highly specific stratification. Past work on ultrasonic characterization of prostate biopsy samples demonstrated obvious attenuation and speed of sound (SoS) differences between normal and cancerous prostate tissue [16]. Work by [15] also showed that the SoS map of ex vivo prostate tissue submerged in a water tank correlates well with MRI-based pathology deduction.

Hardware and image reconstruction for USCT have improved since its debut in the 1970s. Recent research and commercial development have mainly utilized transducer-lined cylindrical water tanks for breast imaging. Two notable systems are the SoftVue by Delphinus [7] and QTScan by QT [14], which was FDA-approved for clinical use in 2017 [18]. Transmission US using these systems has succeeded in characterizing breast density and identifying masses comparable to mammography and tomosynthesis [13], suggesting the value of SoS as a clinical parameter. QT has additionally shown the effectiveness of using inverse scattering to image the human knee [19] and whole body piglet [10] immersed in a scanner tank. While a distal appendage can be easily submerged in a water tank, deep anatomy such as the prostate presents a technical challenge for imaging.

An alternative, dual-robotic approach to USCT of deep anatomy was proposed by Aalimifar, who suggested using software to align two robot-held linear US probes for slice acquisition [1]. This approach circumvents the need for anatomical submersion in a water tank thereby alleviating the size constraints of what can be imaged. While the work proved the feasibility of SoS reconstruction of an agar resected prostate phantom using aligned probes and outlined the calibrations necessary for a dual-robotic approach, it fell short of implementing a practical real-time system for in vivo USCT of the prostate with a TRUS probe. In this paper, we build upon the calibration methods from [1] and develop the first fully functional dual-robot system and clinical workflow to perform USCT of the prostate: one arm holding a physician guided linear TRUS probe for Tx and the other arm autonomously servoing a linear abdominal probe about the patient's pubic region for Rx. Concurrent convex contour tracking and alignment of the abdominal probe in response to TRUS rotations is enforced by our innovative real-time motion framework that works in any unconstrained environment.

2 Materials and Methods

2.1 Proposed General Workflow for Robotic Prostate Tomography

The general proposed clinical setup is shown in Fig. 1, and uses two robots for element-wise sequential Tx and Rx, respectively, and eventual tomographic reconstruction of the prostate: one to steadily hold a TRUS probe transrectally while allowing precise movement along and about the insertional axis (2-DoF), and one to hold a linear abdominal probe externally that autonomously servos (6-DoF) and tracks movement of the TRUS probe to maintain collinear line-of-sight between the probes while enforcing gentle contact with the patient's

pubic region. The TRUS probe can either be controlled collaboratively through physician hand forces or operated with a joystick for precise control.

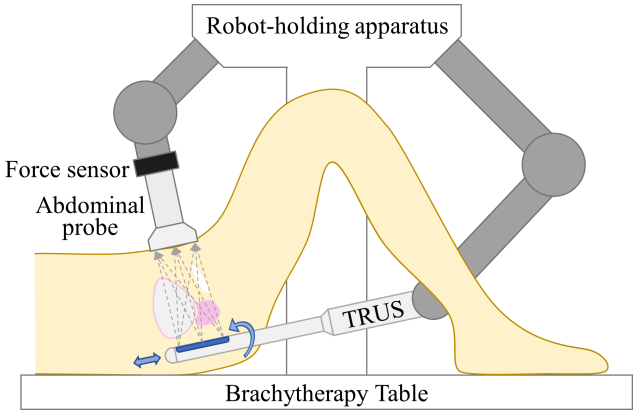

Fig. 1. General approach to dual-robotic USCT. Important anatomy shown in addition to the prostate (pink) includes the bladder (pink outline) which may contain air and the pubic bone (white) which may obfuscate the view of US transmission. (Color figure online)

The clinical workflow is (1) the patient (sedated, as is common for TRUS procedures) lies on a brachytherapy table surrounded by the two robot arms, (2) the physician guides the robotically-held TRUS probe into the rectum until the prostate can be seen on a B-Mode image, (3) coupling gel is generously applied to the pubic region, (4) the software autonomously lowers the robotically-held abdominal probe onto the patient's pubic region in alignment with the TRUS probe, (5) the physician manipulates the TRUS probe while the abdominal probe follows, allowing for continuous US transmission slice acquisition.

In this scheme, the TRUS probe must be the Tx transducer since it is closer to the prostate, allowing the prostate to be more insonated than if the prostate were closer to the Rx transducer, where the acoustic energy is reduced due to scatter. Additionally, the TRUS probe must be the physician controlled element while the abdominal probe is controlled autonomously. This decision was made since every 2-DoF TRUS probe pose has multiple corresponding 6-DoF abdominal probe poses that maintain alignment, whereas the inverse is not guaranteed. This is reasonable for safety and clinical liability since the TRUS probe is invasive.

2.2 Dual Robot Setup and Reference Frames

Two Universal Robots UR5 6-DoF robots were opposingly mounted at 45° on a custom 80/20 T-slot frame as shown in Fig. 2, and controlled by a central compute running software utilizing the open-source CISST/SAW real-time libraries [6]. The two robots used custom 3D printed adapters to hold a BPL9-5/55 linear

TRUS and L14-5W/60 linear abdominal probe respectively. The robot holding the abdominal probe additionally had a 6-DoF Robotiq FT150 force/torque sensor, which was filtered with a low-pass Kalman filter and used for enforcing probe contact against the patient's pubic region. The TRUS probe was connected to an Ultrasonix SonixTouch machine, which sent scanline triggers to a SonixDAQ US acquisition system to which the abdominal probe was connected. Synchronization logic was implemented on an FPGA to only transmit scanline triggers to the DAQ on and after the rising edge of a frame trigger so that US transmission acquisition always started capture with the first elements. A CIRS 048A pelvic phantom was used for algorithm and imaging validation, which had distinct SoS changes between prostate, bladder, pubic bone, and surrounding tissue.

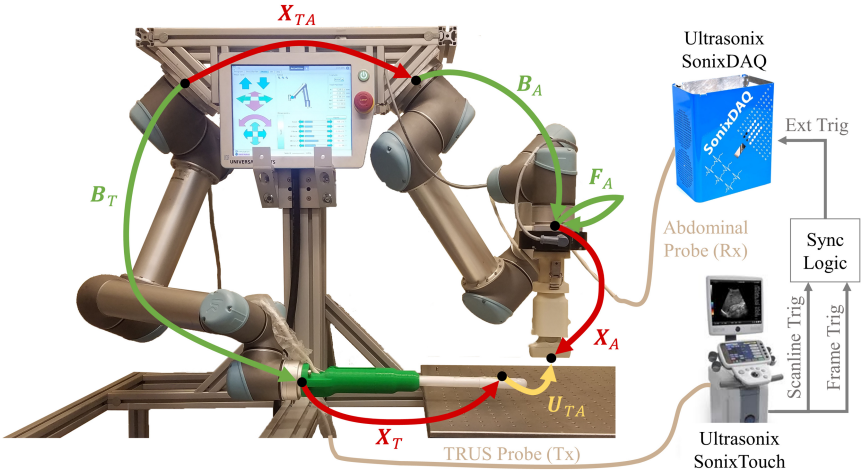

Fig. 2. Experimental setup and frames, including two UR5 robots and their respective US probes and control systems tied together by a synchronized scanline trigger. Transformations in green are known, red (named with X) are unknown and solved through calibration, and yellow are unknown and deduced from the complete kinematic chain. (Color figure online)

The pose of the abdominal probe relative to its robot base can be written $B_A F_A X_A$, where $B_A \in SE(3)$ is the retrievable robot pose, $F_A \in SE(3)$ is the rotational transformation of the robot end-effector to the force/torque sensor, and $X_A \in SE(3)$ is the calibrated transformation to US image-space. Similarly, the pose of the TRUS probe relative to its robot base can be written $B_T X_T$. The transformation from the TRUS probe robot to the abdominal probe robot was called X_{TA}, allowing the relative orientation from the TRUS image-space to the abdominal image-space to be written as $U_{TA} = X_T^{-1} B_T^{-1} X_{TA} B_A F_A X_A$.

2.3 Calibration

The three unknown frame transformations were sequentially calibrated similar to [1]. The transformations from each end effector to its US probe origin, X_A and X_T, were both off-line calibrated by solving separate BXp problems. Specifically, a cross-wire phantom fixed in a water tank was imaged under $N = 60$ independent poses of each robot arm represented by $B_A^{(i)}$ and $B_T^{(i)}$, where $i = 1, \ldots, N$. For each unique pose, the cross location was consistently imaged as a focused spot using each US probe and automatically segmented to get the position of the cross within the 2D US RF signal, $p_T^{(i)}$ and $p_A^{(i)}$. The general BXp problem is given as

$$\underset{X \in SE(3)}{\operatorname{argmin}} \sum_{i=1}^{N-1} \sum_{j=i+1}^{N} \left\| B^{(i)} X p^{(i)} - B^{(j)} X p^{(j)} \right\|_2^2 \tag{1}$$

from which X_A and X_T were respectively optimized through an iterative gradient descent procedure proposed in [2] after algorithm initialization using values attained from measurement with calipers. We withheld $n = 0.1N$ samples of the data to assess calibration accuracy by calculating mean, standard deviation, and max of the Euclidean distance between each calculated cross location and the average cross location.

$$E^{(i)} = \left\| B^{(i)} X p^{(i)} - \frac{1}{n} \sum\nolimits_j B^{(j)} X p^{(j)} \right\|_2 \tag{2}$$

The calibration between robot bases, X_{TA}, was performed by moving the cross-wire phantom to multiple locations, collecting robot poses ($B_T^{(i)}$ and $B_A^{(i)}$) and cross locations ($p_T^{(i)}$ and $p_A^{(i)}$) recorded by each probe. The two point clouds of cross locations are related by $B_T^{(i)} X_T p_T^{(i)} = X_{TA} B_A^{(i)} F_A X_A p_A^{(i)}$, where X_{TA} was solved with Horn's quaternion-based method for $A = XB$ problems [9]. Five non-collinear points were collected to perform the calibration, which was assessed by mean, standard deviation, and max of the Euclidean distance

$$E^{(i)} = \left\| B_T^{(i)} X_T p_T^{(i)} - X_{TA} B_A^{(i)} F_A X_A p_A^{(i)} \right\|_2 \tag{3}$$

2.4 Robot Motion Framework

TRUS probe movements were chosen to be joystick controlled, and were constrained about and along the insertional axis. User-induced joystick movements were converted into commanded velocities via the admittance control algorithm $\boldsymbol{v} = k\boldsymbol{f}$, where k is the constant admittance gain matrix and $\boldsymbol{f}$ was the digitized positional readings from an analog joystick.

Abdominal probe lateral velocities corresponding to TRUS probe movements were calculated using an innovative formulation of hybrid force-position control [11] that achieved real-time, simultaneous abdominal probe alignment and gentle convex contour tracking along the patient's pubic region regardless of body

habitus. Commanded robot velocities were the superposition of two velocity components, $\boldsymbol{v}_{cmd} = \boldsymbol{v}_{pose} + \boldsymbol{v}_{contact}$, as shown in Fig. 3. Robot Cartesian velocity $\boldsymbol{v}_{pose}$ was needed to reorient the abdominal probe to be collinear with the TRUS while not having any velocity in the y-direction (toward the patient). The velocity resulted from first calculating the goal transformation $U_{TA'}$ that defined what U_{TA} should approach for the two probes to be perfectly collinear without any probe y movement. $U_{TA'}$ was formulated in homogeneous coordinates as

$$U_{TA'} = \begin{bmatrix} 1 & 0 & 0 & \\ 0 & -1 & 0 & \boldsymbol{p}_I \\ 0 & 0 & -1 & \\ 0 & 0 & 0 & 1 \end{bmatrix} \tag{4}$$

which constitutes a 180° rotation about the x-axis (to preserve alignment) and a translation equal to the intersection point $\boldsymbol{p}_I$ of the TRUS line-of-sight vector with the plane formed by the abdominal probe transducer face (to nullify any y movement). Once calculated, the new desired abdominal probe robot orientation was calculated as $B_{A'} = X_T^{-1} B_T X_T U_{TA'} X_A^{-1} F_A^{-1}$ from which $\boldsymbol{v}_{pose}$ was calculated through a PID loop for smoothing and scaling. Robot Cartesian velocity $\boldsymbol{v}_{contact}$ was needed to enforce probe coupling with the acoustic gel and accomplish convex contour tracking. It was calculated using impedance control

$$\boldsymbol{v}_{contact} = K(F_D - F) - D(\dot{F}) \tag{5}$$

with stiffness K, damping D, desired force F_D which was only nonzero for contact force, and Kalman-smoothed force measurements F arriving 125 Hz. The impedance control gains were manually tuned so that the probe "hovered" on the gel pad without applying excessive force to the phantom.

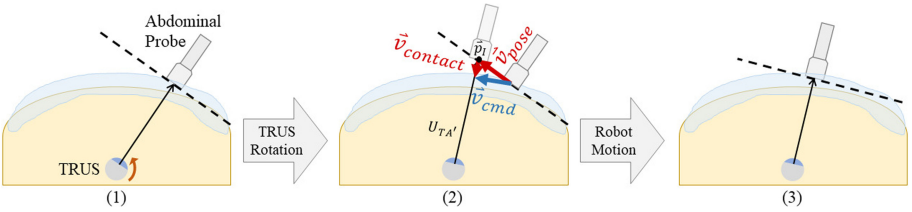

Fig. 3. Proposed robot motion framework for abdominal probe alignment and contour tracking following a TRUS movement, shown on an axial pelvic slice: (1) Initial setup. (2) Two distinct velocity vectors arising from the plane-axis intersection constraint and impedance control, and their superposition that was commanded to the robot. (3) Result of commanding velocities for a short duration.

3 Results

3.1 Calibration

The accuracy of X_A and X_T was assessed by (2) using withheld test data, resulting in $\overline{E} = 0.13\,\text{mm} \pm 0.08\,\text{mm}$, $0.52\,\text{mm} \pm 0.30\,\text{mm}$ respectively, and

$\max\{E\} = 0.26\,\text{mm}$, 1.08 mm respectively. Repeating calibration and testing with shuffled datasets yielded similar results. The accuracy of X_{TA} was assessed by (3), resulting in $\overline{E} = 0.58\,\text{mm} \pm 0.32\,\text{mm}$ and $\max\{E\} = 1.01\,\text{mm}$.

These sub-millimeter individual calibration accuracies, also considering the repeatability of both robots (0.1 mm), exceeds the accuracy of [1] and is therefore acceptable for tomography by their proposed standard. The accuracy difference between the linear abdominal and TRUS probe calibrations is explained by the longer TRUS probe lever-arm and difficulty of maneuvering it into unique configurations within a water tank.

3.2 Robot Motion Framework

We validated our motion framework by collecting orientation and force metrics while rotating the TRUS probe within the pelvic phantom such that the abdominal probe laterally traversed the pelvic region once. An axial projection of abdominal probe Cartesian positions and orientations on the phantom surface with respect to a stationary coordinate frame (defined as the initial frame of the TRUS probe) is shown in Fig. 4a, where the probe is observed to smoothly trace a 2^{nd}-degree polynomial approximation of the convex phantom pelvic region while successfully maintaining probe collinearity throughout. The subtle movement of the TRUS probe while rotating can be attributed to slight X_T calibration inaccuracy amplified over the length of the TRUS probe.

The detected force magnitudes during the traversal are shown in Fig. 4b, and averaged $2.15N \pm 0.15N$. Detected torque magnitudes were negligible and averaged $0.07N{\cdot}m \pm 0.03N{\cdot}m$. These results clearly indicate a stable motion framework, since the abdominal probe maintained continuous contact with the coupling gel while tracing the pubic contour and applied constant, gentle forces to the phantom without palpating. The abdominal probe was observed to "hover" on the generously applied gel pad during its traversal as designed without abraising, tugging, or indenting the phantom surface. This is desirable for patient comfort and air bubble avoidance, and ensures that our framework is robust to varying pubic region curvatures and subcutaneous fat compliances across patients. Our validated approach to real-time autonomous probe servoing in an unconstrained environment could also have implications for adding autonomy to any robot-assisted US procedure, such as remote lung imaging in the ICU.

3.3 Imaging

We tested the feasibility of collecting transmission US slices of our pelvic phantom for USCT using our novel dual-robotic rectum-to-abdomen imaging approach. Most importantly, we qualitatively verified that a suitable anatomical window through the prostate exists that is not obfuscated by the dense pelvic bone when the probes are aligned along the mid-sagittal plane. The window is illustrated in the manual overlay of two captured, opposing B-mode images in Fig. 4c. We also quantified the number of prostate slices that could be acquired by our tomographic setup, which is proportional to the attainable quality of SoS

reconstruction. Figure 4a shows that the TRUS probe was only able to rotate about 23.3° total, which would theoretically allow 46 slices to be acquired for our 720 CPR motor encoder. It is difficult to deduce if this is sufficient for reconstruction and further verification is needed.

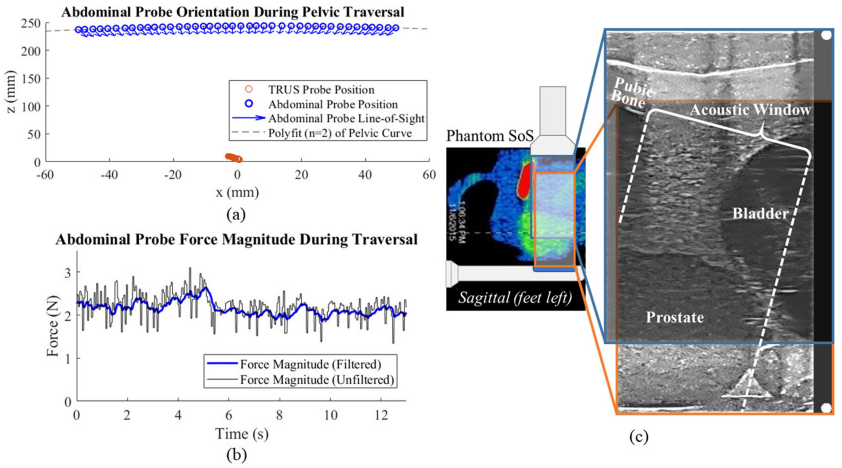

Fig. 4. (a) Abdominal probe Cartesian positions and orientations on the pubic region while rotating the TRUS probe, projected into 2-D and downsampled for clarity. Arrows show abdominal probe line-of-sight. (b) Abdominal probe force magnitudes while performing the lateral pelvic traversal in Fig. 4a. (c) Overlay of B-mode images acquired by both probes showing an acoustic window for transmission US of the prostate.

4 Discussion and Conclusions

The innovative dual-robotic setup, workflow, precise calibrations, and robot motion framework that we developed and validated is clinically feasible for US slice acquisition of the prostate towards tomographic reconstruction. Our evaluation methodology and reported metrics show proper functionality of the developed robot setup and motion framework, and confirm that an US transmission window through the prostate can be found without interference from the pubic bone. Additionally, while it is difficult to quantify the overall system accuracy needed for USCT since transmission US of the in vivo prostate by these means has not been attempted before, we believe that the sub-millimeter accuracy attained by our individual calibrations are sufficient for SoS mapping.

The main limitation of a dual-robotic USCT approach is the need for an accurate three-way calibration of the two probes and robots. Future work should include an improved active element calibration scheme for X_A and X_T, as well as an alternative calibration scheme for X_{TA} that isolates it from errors propagated

by X_A and X_T, such as a pivot calibration about a fixed point. In-plane and out-of-plane accuracy should also be distinguished and exact angular error should be computed. We are additionally interested in a novel on-line calibration fine-tuning scheme for X_{TA}, in which the TRUS probe emits periodic pulses and the receiving abdominal probe, acting as a hydrophone, uses gradient descent guided motion to centralize itself directly within the TRUS probe's line-of-sight.

Using our system, future work should focus on implementing and enhancing limited-angle tomographic reconstruction methods to build accurate SoS maps from collected US data. Deep learning approaches [3,5] may greatly improve the image quality. It is our ultimate hope that, when applied in a human trial, the slices collected by our accurate dual-robotic US system will produce SoS mappings that significantly improve prostate cancer diagnosis and staging.

References

1. Aalamifar, F.: Co-robotic ultrasound tomography: a new paradigm for quantitative ultrasound imaging. Ph.D. thesis, Johns Hopkins University, October 2016
2. Ackerman, M.K., Cheng, A., Boctor, E., Chirikjian, G.: Online ultrasound sensor calibration using gradient descent on the Euclidean group. In: 2014 IEEE International Conference on Robotics and Automation (ICRA), pp. 4900–4905 (2014)
3. Anas, E.M.A., et al.: CNN and back-projection: limited angle ultrasound tomography for speed of sound estimation. In: Medical Imaging 2019: Ultrasonic Imaging and Tomography, vol. 10955, p. 109550M. International Society for Optics and Photonics (2019)
4. Bray, F., Ferlay, J., Soerjomataram, I., Siegel, R.L., Torre, L.A., Jemal, A.: Global cancer statistics 2018: GLOBOCAN estimates of incidence and mortality worldwide for 36 cancers in 185 countries. CA Cancer J. Clin. **68**(6), 394–424 (2018)
5. Cheng, A., et al.: Deep learning image reconstruction method for limited-angle ultrasound tomography in prostate cancer. In: Medical Imaging 2019: Ultrasonic Imaging and Tomography, vol. 10955, p. 1095516. International Society for Optics and Photonics (2019)
6. CISST libraries and Surgical Assistant Workstation (SAW). https://github.com/jhu-cisst/cisst/wiki
7. Delphinus Medical Technologies: Softvue system (2020). http://www.delphinusmt.com/technology/. Accessed 11 Mar 2020
8. Harvey, C., Pilcher, J., Richenberg, J., Patel, U., Frauscher, F.: Applications of transrectal ultrasound in prostate cancer. Br. J. Radiol. **85**(Spec. Issue 1), S3–S17 (2012)
9. Horn, B., Hilden, H., Negahdaripour, S.: Closed-form solution of absolute orientation using orthonormal matrices. J. Opt. Soc. Am. A **5**, 1127–1135 (1988). https://doi.org/10.1364/JOSAA.5.001127
10. Lenox, M., et al.: 3D inverse scattering in wholebody ultrasound applications (conference presentation). In: Medical Imaging 2019: Ultrasonic Imaging and Tomography, vol. 10955, p. 1095511. International Society for Optics and Photonics (2019)
11. Lozano, R., Brogliato, B.: Adaptive hybrid force-position control for redundant manipulators. In: 29th IEEE Conference on Decision and Control, vol. 3. pp. 1949–1950 (1990)

12. Marks, L., Young, S., Natarajan, S.: MRI-ultrasound fusion for guidance of targeted prostate biopsy. Curr. Opin. Urol. **23**(1), 43 (2013)
13. Natesan, R., Wiskin, J., Lee, S., Malik, B.H.: Quantitative assessment of breast density: transmission ultrasound is comparable to mammography with tomosynthesis. Cancer Prev. Res. **12**(12), 871–876 (2019)
14. QT Ultrasound: Quantitative transmission ultrasound: an evolution in breast imaging (2020). https://www.qtultrasound.com/about-us/. Accessed 11 Mar 2020
15. Seifabadi, R., et al.: Correlation of ultrasound tomography to MRI and pathology for the detection of prostate cancer. In: Medical Imaging 2019: Ultrasonic Imaging and Tomography, vol. 10955, p. 109550C. International Society for Optics and Photonics (2019)
16. Tanoue, H., Hagiwara, Y., Kobayashi, K., Saijo, Y.: Ultrasonic tissue characterization of prostate biopsy tissues by ultrasound speed microscope. In: 2011 Annual International Conference of the IEEE Engineering in Medicine and Biology Society, pp. 8499–8502. IEEE (2011)
17. Wallis, C.J., Haider, M.A., Nam, R.K.: Role of mpMRI of the prostate in screening for prostate cancer. Transl. Androl. Urol. **6**(3), 464 (2017)
18. Wiskin, J., et al.: Full wave 3D inverse scattering transmission ultrasound tomography: breast and whole body imaging. In: 2019 IEEE International Ultrasonics Symposium (IUS), pp. 951–958. IEEE (2019)
19. Wiskin, J.W., Malik, B., Natesan, R., Pirshafiey, N., Klock, J., Lenox, M.: 3D full inverse scattering ultrasound tomography of the human knee (conference presentation). In: Medical Imaging 2019: Ultrasonic Imaging and Tomography, vol. 10955, p. 109550K. International Society for Optics and Photonics (2019)